# An Examination of Unsteady Airloads on a UH-60A Rotor: Computation versus Measurement

Robert T. Biedron
Senior Research Scientist

Elizabeth M. Lee-Rausch
Research Engineer

*NASA Langley Research Center, Hampton, VA 23681*

**An unsteady Reynolds-averaged Navier-Stokes solver for unstructured grids is used to simulate the flow over a UH-60A rotor. Traditionally, the computed pressure and shear stresses are integrated on the computational mesh at selected radial stations and compared to measured airloads. However, the corresponding integration of experimental data uses only the pressure contribution, and the set of integration points (pressure taps) is modest compared to the computational mesh resolution. This paper examines the difference between the traditional integration of computed airloads and an integration consistent with that used for the experimental data. In addition, a comparison of chordwise pressure distributions between computation and measurement is made. Examination of this unsteady pressure data provides new opportunities to understand differences between computation and flight measurement.**

## Nomenclature

| | |
|---|---|
| $()_{tip}$ | denotes blade tip |
| $\mu$ | advance ratio |
| $\psi$ | azimuthal position [°] |
| $\rho_\infty$ | freestream density [slugs/ft$^3$] |
| $\sigma$ | solidity |
| $a_\infty$ | freestream speed of sound [ft/s] |
| $c$ | local blade chord [ft] |
| $C_T$ | thrust coefficient $(\frac{T}{\rho_\infty {V_{tip}}^2 \pi R^2})$ |
| $F_c$ | sectional chord force [lb/ft] |
| $F_n$ | sectional normal force [lb/ft] |
| $M_y$ | $c/4$ sectional pitching moment [lb] |
| $M_\infty$ | freestream Mach number $(\frac{V_\infty}{a_\infty})$ |
| $R$ | rotor radius [ft] |
| $r$ | radial position [ft] |
| $T$ | thrust [lb] |
| $V_\infty$ | freestream velocity [ft/s] |
| ${M_\infty}^2 C_c$ | sectional chord force coefficient $(\frac{F_c}{\frac{1}{2}\rho_\infty {a_\infty}^2 c})$ |
| ${M_\infty}^2 C_m$ | $c/4$ sectional pitching moment coefficient $(\frac{M_y}{\frac{1}{2}\rho_\infty {a_\infty}^2 c^2})$ |
| ${M_\infty}^2 C_n$ | sectional normal force coefficient $(\frac{F_n}{\frac{1}{2}\rho_\infty {a_\infty}^2 c})$ |
| $()_\infty$ | denotes freestream condition |
| CFD | Computational Fluid Dynamics |
| CSD | Computational Structural Dynamics |

Presented at the American Helicopter Society 68th Annual Forum, Fort Worth, TX, May 1-3, 2012. 

## Introduction

Significant progress has been made in the last decade toward meeting the challenge of predicting rotor airloads by coupling Computational Fluid Dynamics (CFD) with Computational Structural Dynamics (CSD). Various research groups have coupled a range of CFD codes (including structured-grid, unstructured-grid, Cartesian-grid solvers) to a number of different CSD codes. In some cases, the

same CFD code has been coupled to more than one CSD code. Two long-running workshops, the UH-60A Airloads Workshop and the International HART-II Workshop, have provided forums for comparison of computed results for a common configuration obtained with different solution methodologies. First presented at a UH-60A Airloads Workshop, three recent simulations of the UH-60A Blackhawk rotor have produced remarkably similar results for conditions spanning the flight envelope, despite using quite different CFD and CSD codes, different grid resolutions, and different time steps (Ref. 1). Differences in sectional airloads between the various simulations are considerably smaller than the difference between the simulations and flight measurements.

Although the comparison of these CFD/CSD results with UH-60A flight data may be viewed as being "reasonable" considering the complexity of the problem, they are still less than completely satisfactory. Pitching moment in particular often exhibits a significant mean-value offset between computation and flight. The computed chord force also tends to exhibit significant offset from flight. There are many possible reasons for discrepancies between flight and computation. Between the need to account for both aerodynamics and structural dynamics, there is ample opportunity for modeling errors. For example, numerical resolution may be insufficient; rotor trim targets are estimates, not measured directly; and structural properties may not be known precisely. The authors previously explored the sensitivity of computed results to CFD parameters such as mesh size, time step, and turbulence model (Ref. 2); relatively little sensitivity was observed, particularly for a high-speed case. This paper examines whether the difference in integration method employed for the measured data and the computed data contributes to the observed discrepancies. Computed solutions are integrated to provide sectional airloads using exactly the same method, and in fact the same code, as used for the measured flight data. An additional outcome of this consistent integration is that unsteady pressure distributions are compared between computation and flight. To the authors' knowledge, both are unique aspects of the current paper that have not been examined before.

## Flight-Test Data

During 1993–1994, flight tests of a highly instrumented UH-60A were conducted as part of the joint NASA-Army UH-60A Airloads Program (Ref. 3). One blade was instrumented with unsteady pressure transducers, and a second blade was instrumented with strain gauges and accelerometers. Data were collected for multiple flight conditions, referred to as "counters", at a large number of points within the flight envelope, including high-speed flight and dynamic stall. The wealth of data from this test has been extraordinarily beneficial to the development and validation of rotorcraft simulation codes. However, due to the nature of flight testing, some important information is either not available from flight or can only be estimated. For example, main rotor thrust was determined based on estimates of vehicle weight during the particular flight counter, estimates of downwash loading on the fuselage, and estimates of tail rotor loading. Like most rotor blades, those of the UH-60A undergo significant deformation as the blades rotate. While the pressure transducers provided means of assessing sectional aerodynamic loading, corresponding blade deflections, crucial to a more complete validation of prediction methods, were not measured during this flight test.

## CFD/CSD Methodology

The unstructured-grid flow solver used for this study is FUN3D (Refs. 4, 5). The code solves the unsteady Reynolds-Averaged Navier-Stokes equations, with several models available for turbulence closure. The solver has a variety of mesh-motion options, including rigid, deforming, and overset meshes, and a robust implicit time-advancement scheme (Ref. 6). For overset meshes, the DiRTlib (Ref. 7) and SUGGAR++ (Ref. 8) codes are used to facilitate communication between disparate zones in the mesh. Aeroelastic effects and trim are accounted for via coupling with a rotorcraft comprehensive code (Refs. 2, 9, 10). The coupling is implemented via the loose coupling strategy outlined by Potsdam et al. (Ref. 11), and thus is appropriate to steady, level flight.

The rotorcraft CSD code used for this study is CAMRAD II (Ref. 12). The aerodynamics modules within CAMRAD II are based on lifting-line models that use airfoil tables, coupled with wake models. Although such aerodynamic models can provide reasonable results for many flight conditions, in some cases the predictions of the airloads can be inaccurate because of limitations of the relatively low-order aerodynamic modeling. When converged, the loose coupling approach replaces the low-order lifting-line aerodynamics of the CSD code with the higher-fidelity Navier-Stokes aerodynamics of the CFD code (Refs. 9, 11). Within CAMRAD II, each blade is modeled as a set of nonlinear beam elements. In addition to the structural dynamics modeling, CAMRAD II offers a sophisticated trim capability. For the UH-60A simulations in this paper, a three-degree-of-freedom trim is used, with the (solidity-weighted) thrust coefficient, pitching moment, and rolling moment specified as trim targets within CAMRAD II.

## Evaluation of Sectional Airloads

In the flight-test program, one blade of the vehicle was instrumented with 241 unsteady pressure transducers. Transducers were generally grouped chordwise along nine radial stations. A maximum of 15 transducers were installed on

the upper-surface at each radial station, along with a maximum of 15 transducers on the lower-surface at each station. Although the transducers were clustered near the leading edge to better resolve the pressure distribution there, the number of points used to integrate the measured data were sparse in comparison with the number of points typically used for integration of CFD data. Furthermore, not all transducers remained operational for all for the run conditions of the flight-test program. Post-test examination of transducer output resulted in some marked as unreliable,[1] and nonfunctional or unreliable transducer data were not used for integration of the measured pressures. There were no transducers located at either the leading or trailing edges. Aerodynamic shear stresses were not measured, so integrated sectional airloads reflect only the pressure contribution. Integration of the pressure data was handled by the TRCPCL code.[2] This code reads a file containing pressure data from each of the taps (referred to herein as a "TP" file), together with a file denoting the status of the pressure tap during the particular flight test (a "PSTATUS" file). For example, some taps may not be installed at a particular station, or the data for a particular tap may have been deemed unsatisfactory when examined after the test. If a tap is not installed or its data otherwise deemed unreliable, that pressure is excluded from the integration. If fewer than five reliable pressure taps are available on either the upper or lower surface, the integration for that section is skipped. Pressures are integrated in a mapped coordinate system, using a $2^{nd}$ order integration scheme. For the mapped integration, pressures are multiplied by $(x/c)^{0.5}$ and then integrated as a function of $(x/c)^{0.5}$. This mapping takes advantage of the transducer clustering near the leading edge and removes the need for pressure data at the leading edge. To provide closure of the pressure distribution at the trailing edge, TRCPCL uses an average of the nearest valid upper and lower surface pressure data. In certain instances, the nearest valid tap may be located a large distance away from the trailing edge.

As part of the CFD/CSD coupling process, FUN3D performs an intersection of the blade surface with a cutting plane at user-specified radial stations. At these intersected blade sections, the leading and trailing edges of the local section are determined, from which the local blade twist angle and quarter-chord location are found. This intersection process also determines the location of points used to integrate the CFD solution. Because of the unstructured triangulation of the blade surface, the number of integration points will vary slightly from station to station. For the typical mesh densities used in this study, on the order of 250 points are used for integration at each station as opposed to the maximum of 30 integration points available from the pressure taps. Because the computational mesh points are clustered around the leading and trailing edges, the integration points will be clustered there too. Within FUN3D, the pressure and shear-stress components are integrated in a blade-oriented coordinate system. Optionally, the pressure and shear-stress components, together with the local twist angle and quarter-chord position may be output to a file. Once the sectional integration in the blade-aligned system is complete, the forces and moments are transformed to a section-aligned system by rotation through the local twist angle. Forces and moments are transferred to CAMRAD II in the section-aligned coordinate system. This "native" integration of the CFD solution to determine sectional airloads includes both pressure and shear-stress contributions.

To facilitate a direct comparison with the measured-data integration, the CFD data from FUN3D was converted into a TP file, exactly analogous to that associated with the measured flight data. This was accomplished by using the existing optional output mentioned above, and linearly interpolating the pressures to the blade tap locations used in the measurements. This TP file of computed results, together with the PSTATUS file for the particular test conditions, was processed using the TRCPCL code. In this manner only active/valid tap locations are used for CFD integration. With both computed and measured pressure data in the same file format, a direct comparison of the unsteady pressure distributions can be made.

### Comparison with High-Speed Flight Data - C8534

First, computational results are shown for conditions corresponding to the flight-test counter 8534. This case has become a canonical case for CFD/CSD validation and is the most widely simulated condition in the UH-60A Airloads Database. It corresponds to a solidity-weighted thrust coefficient of $C_T/\sigma = 0.081$ at an advance ratio $\mu = 0.365$ with a (hover) tip Mach number of $M_{tip} = 0.642$. This condition represents the highest level-flight speed in the UH-60A Airloads Database, as well as the flight condition with the highest vibration levels.

The numerical simulations presented here were carried out for an isolated rotor using a mesh containing approximately 15 million nodes (Ref. 2). Mesh cells near the blade surface are prismatic and transition to tetrahedra away from the surface. A time step corresponding to $1^\circ$ change in rotor azimuth was used, and the Spalart-Allmaras turbulence model (Ref. 13) was employed. Further details of the numerical simulations, as well as an examination of the sensitivity of the results to mesh size, time step, and turbulence model were examined in previous work (Ref. 2)

[1]Bousman, W.; U.S. Army Aeroflightdynamics Directorate, Moffett Field, CA, Private Communication, August 2011

[2]Bousman, W.; U.S. Army Aeroflightdynamics Directorate, Moffett Field, CA, Private Communication, December 2010

where sectional airloads (normal force, pitching moment, and chord force) were found to be insensitive to the aforementioned parameters. In the figures pertaining to sectional airloads presented here, computed results labeled "CFD" correspond to the results presented in this earlier work, using the native integration method described above. Computational results labeled "CFD / TRCPCL" use the TRCPCL code to integrate only pressure at valid tap locations. Below, comparisons with pressure data are shown "on the advancing side" and "on the retreating" side of the rotor disk. For purposes of figure grouping, the zero azimuthal station (aligned with the fuselage axes, downwind) is grouped as part of the advancing side, while 180° azimuth is grouped as part of the retreating side.

Figure 1 illustrates the radial stations at which test data were collected on one of the rotor blades. Because detailed pressure data can be compared at many azimuthal positions for each radial station, only a small set of computed vs. measured comparisons can be shown within the space constraints of this paper. Two stations, $r/R = 0.675$ and $r/R = 0.865$ are examined in this paper; these stations are indicated in red in Figure 1. Of these two stations, the more outboard one is examined in slightly more detail, as the aerodynamics are more varied at that location. Furthermore, $r/R = 0.865$ is a station at which integrated airloads have been examined by many, if not most, previous computational studies. Integrated sectional airloads from CFD/CSD and test are shown in coefficient form for normal force, pitching moment, and chord force vs. rotor azimuth. Pitching moment is positive nose up, chord force is positive directed toward the trailing edge, and normal force is positive up. Computed airloads are shown for both the native and TRCPCL integration methods. Means are not removed from the integrated airloads to better assess the effect of the integration method on the computed results. Measured and computed pressures versus $x/c$ are shown at the selected radial stations, principally for 45° increments around the rotor disk.

Figure 2 shows the comparison between rotor airloads from flight and computation at $r/R = 0.675$. At this station, there is very little difference in either computed normal force or computed pitching moment using either the native integration or using the TRCPCL code. Although the variation of the pitching moment with azimuth is reasonably captured by the computation, there is an offset from the flight data; this offset is essentially unchanged by the integration method. However, there is considerable sensitivity of the computed chord force to the integration procedure on the advancing side, with the TRCPCL-integrated result significantly closer to the TRCPCL-integrated flight data. Recall that the TRCPCL integration of computed results removes any skin-friction contributions because skin-friction contributions were not included during the flight test measurements. A separate "native" integration the pressure and skin-friction contributions has not been carried out for each section. However, spot checks of total integrated forces on individual rotor blades, for which the contributions of pressure and skin friction are separately accounted, show that indeed the skin friction contribution to the in-plane force can be quite significant, on the order of 20 per cent on the advancing side for C8534.

A comparison of the corresponding chordwise (gauge) pressure distributions at $r/R = 0.675$ for a small set of azimuthal positions is shown in Figures 3 and 4. Generally speaking, the agreement between the measured and computed pressures is good, except for 90° on the advancing side. Here the poorest agreement is on the upper surface where the measured peak suction pressure is roughly 2 psi lower (more negative) than the computed pressure. Pressure levels on the lower surface are generally in good agreement with the measured data, except near the leading edge where the flight pressure distribution in not as smooth as the computed distribution.

Figure 5 shows the comparison between rotor airloads from flight and computation further outboard at $r/R = 0.865$. There are a few small differences in normal force and pitching moment between computational results integrated with TRCPCL and those using native integration. But once again the principal difference is in chord force on the advancing side, and by using TRCPCL to integrate only the pressure contribution from the computation yields significantly better correlation with the flight data.

Figure 6 shows pressures on the advancing side for $r/R = 0.865$ at finer azimuthal increments of 15°. The finer azimuthal resolution compared to Figure 2 is used to better visualize the motion of the shock wave that is present at this station on the advancing side. Beginning at 0°, the computed and flight pressures are in very good agreement. Indeed until an azimuth of 45° the agreement is fairly good, except for an odd spike in the measured pressures around $x/c = 0.2$. By 45° however, a shock has formed on the upper (suction) surface, and although captured by the CFD solution, the predicted shock location is too far forward, and slightly weaker than flight measurement. Through 90°, the pre-shock suction pressure on the upper surface remains nearly constant, while the computed peak suction pressure drops after 75°, and the computed shock position remains too far forward. In the measured data on the advancing side, the pressure tap at $x/c = 0.2$ remains slightly suspect, judged by pressures at neighboring taps. However, on the retreating side the pressures at that location do not stand out from neighboring pressures. By 105° the lower surface has larger suction pressures than the upper surface, a fact that is also reflected in the negative normal force at this azimuth in Figure 5. The computed and measured lower surface pressures are again in reasonably good agreement, though the computed lower surface shock position is still slightly forward of the measured one. Larger discrepancies remain on

the upper surface; computed pressures do not suggest an upper-surface shock, though one appears present in flight at 105°. By 135°, the computed and measured pressures are in reasonably good agreement on both surfaces. The lower surface suction peak has largely disappeared by 150°, and the upper surface is on the way to again becoming the primary suction surface, a transition completed by 165°, and leading once again to a positive normal force. Note that despite the rather significant differences in shock positions in the region between 45° and 90°, the integrated normal force from the computation is in very good agreement with the flight data. Even the pitching moment is in remarkably good agreement considering the shock differences. Compensating differences have been masked through integration. In this case, differences between computation and flight only become evident upon closer inspection of the pressure data.

Figure 7 shows the pressure distribution at four azimuthal locations on the retreating side for this radial station. The agreement between computed and measured pressure distributions on the retreating side is generally better than on the advancing side, although peak suction pressures are higher in the flight data.

### Comparison with High-Thrust Flight Data - C9017

The second flight counter considered for comparison is C9017. This counter corresponds to a solidity-weighted thrust coefficient of $C_T/\sigma = 0.129$ at an advance ratio $\mu = 0.237$ with a (hover) tip Mach number of $M_{tip} = 0.666$. The high thrust coefficient places this flight condition near the stall boundary. This flight condition represents a more challenging computation, and computed results are more sensitive to numerical modeling than C8534. For this high-thrust flight condition, several radial stations exhibit double dynamic-stall events on the retreating side.

As for C8534, the effect of integration method on the computed airloads is first examined in Figure 8 for $r/R = 0.675$. Once again the integration method has relatively little effect on the normal force and pitching moment, and a significant effect on the chord force on the advancing side. A relatively mild stall is evident on the retreating side as a reduction in normal force and drag, and an increase in nose-down (negative) pitching moment starting near 195°.

Chordwise pressure distributions at $r/R = 0.675$ are shown in Figures 9 and 10 for four azimuthal stations on both the advancing and retreating sides. Peak suction pressure levels on the upper surface are well predicted for 0° and 45°, but at 90°, the computation predicts a lower peak suction, located further forward than observed in flight. The measured pressures tend to show a slightly larger aft loading than the computed pressures downstream of the suction peak to approximately 80 percent chord. On the retreating side, the pressure distributions reflect the stall evident in the integrated airloads. At 180°, the suction peak is relatively large, but the shape is characteristic of fully attached flow. By 225° however, a reduced suction peak and flat loading over the aft portion of the blade are indicative of separated flow. Once the blade has reached 270° and 315°, the pressure distributions are again indicative of attached flow.

Of the stations exhibiting double dynamic-stall events, the ones at $r/R = 0.865$ are the most severe. Figure 11 shows the sectional airloads at this station for both computation and flight. The computed normal force and pitching moment compare less favorably with the flight data at this radial station than the corresponding C8534 data, and for the pitching moment there is a large but fairly constant offset between computation and flight. The two dynamic-stall events are perhaps most clearly observed in the increase in nose-down (more negative) pitching moment that begins around 240° and again near 315°. Precipitous drops in the normal and chord force are also readily observable at these locations. Once again, the only significant change in computed airloads using pressure integration at functional transducer locations is in the chord force on the advancing side, where a consistent integration improves the correlation. In particular, using a consistent integration does not remove the significant offset in pitching moment.

Figure 12 illustrates the pressures at four azimuthal locations on the advancing side. As expected from the integrated airloads, the comparison of pressure distributions between computation and flight is not as favorable as for C8534. For the high-speed case, pressure distributions at 0° compared well between computation and flight; but for the high-thrust condition, the comparison is not nearly as favorable. By 45°, a shock is evident on the upper surface with both the strength and location correctly captured in the computation. The suction peak on the lower surface is not well captured by the computation. At an azimuth of 90°, the computation (as for the high-speed case) misses the peak suction pressure on the upper surface, and predicts the shock location too far forward. The computed peak suction pressure on the lower surface is much further forward than the corresponding location in the data. By 135° the upper-surface shock has subsided in both computation and flight, although the comparison of pressures is otherwise not very favorable. Notably, the significant aft loading observed in the flight pressures at all azimuthal locations is not seen in the computed pressures, which in turn leads to a more nose-down (negative) pitching moment in the flight data, as reflected in Figure 11. Note that $r/R = 0.865$ is the most outboard station with the tab extension (see Figure 1), and is very near the tab / no tab juncture. One possible explanation for the observed differences in aft loading between computation and flight is that the local section geometries differ sufficiently to affect the results for high-thrust.

For the retreating side, Figure 13 shows the pressure distributions at finer azimuthal increments (15°) to provide a

better resolution of the two dynamic-stall events. As on the advancing side, the significantly higher aft loading of the flight pressures is evident from the large pitching moment offset. The pressure distributions between 180° and 240° do not vary significantly with azimuth. Apart from the larger aft loading, flight pressures on the upper surface are noticeably less smooth than the corresponding computational distributions. This "lumpiness" in the distribution, aft of $x/c = 0.2$, is quite persistent between these azimuthal locations. Whether this is a real effect missed by the computations, or some artifact of the measurement is unknown. However, at 255°, the signature of a vortex, associated with the first dynamic stall, is seen near $x/c = 0.4$ as a local increase in suction pressure. The effect is seen in both computation and flight, although it is more pronounced, and slightly more downstream (approximately 0.1 chord) in the flight data. By 270°, the stall is essentially complete and the section has lost much of its lift. Lift is increasing again by 300°. At 315°, a local suction increase due to a vortex from the second dynamic stall is evident in the flight data, but not in the computational data. This appears consistent with the sectional airloads shown in Figure 11 where, judging from the pitching moment response, the second dynamic stall in the flight data begins roughly 15° ahead of the computed one. Not until 330° do the computed pressures even begin to hint at a passing vortex, with a very slight flattening of the loading around $x/c = 0.3$.

## Concluding Remarks

From the comparisons made to date, the relatively sparse set of pressure taps used as input to the TRCPCL integration code *does not* contribute significantly to previously-observed discrepancies between flight and computation for sectional normal force and pitching moment. Sectional chord force however, *does* show a significant effect from the integration method, particularly on the advancing side of the rotor disk.

Prior computational efforts, including those of the present authors, have focused primarily on sectional airloads when comparing with aerodynamic data from the 1993–1994 Airloads Program. However, a wealth of data from the Airloads Program in the form of the "raw" pressure data has seemingly not been used to further understand the differences between computation and flight. This paper examined only a tiny fraction of the available pressure data: two radial stations for both a high-speed and high-thrust case. Even within this limited scope, only a relatively few azimuthal could be presented.

A close examination of unsteady pressure data for C8534 at $r/R = 0.865$ has revealed important differences in computed shock strength and position relative to flight data. These differences are not readily apparent when looking at integrated sectional airloads at that station. Indeed, the $r/R = 0.865$ station for C8534 is one of the points for which correlation between computation and flight has historically been considered quite good in terms of integrated sectional airloads. Recent comparisons of widely differing CFD/CSD systems showed nearly identical results in terms of integrated sectional airloads to those for the FUN3D/CAMRAD II results presented here, so it would be instructive to look at corresponding pressure distributions in other CFD/CSD results.

For the high-thrust case, C9017, observed differences in the pressure distributions between computation and flight were less surprising since the integrated sectional loads had previously shown less favorable comparison with flight measurements relative to the high-speed case. The examination of pressures revealed that the flight pressures exhibited considerably more aft loading than the computational pressures. In addition, the footprint of the leading-edge vortex resulting from the dynamic stall is not nearly as prominent in CFD as in the flight data. This is consistent with the more nose-down pitching moment seen in the integrated data from flight compared to computation. However, when considering only the integrated airloads, the source of the discrepancy is masked.

At the present time, the reasons for the observed differences in pressure distributions between flight and computation are unclear. Previous studies have indicated a very small sensitivity in computed (integrated) airloads to CFD modeling parameters for the high-speed case. Subtle geometry differences in critical regions (e.g., the extension tab) between the computational model and the as-built rotor may contribute, particularly for a high-thrust situation. In addition, measured data is subject to some uncertainties. For example, anomalous behavior of certain pressure taps is occasionally apparent on the advancing side, but not the retreating side. Of course, the fact that aerodynamics and structural dynamics are intimately coupled in rotorcraft systems makes assessing such differences difficult without further data. Near-future plans include a similar examination of recently-completed wind-tunnel tests of the same UH-60A rotor (Ref. 14), for which both pressure and deflection data will be available.

## Acknowledgment

The authors would like to thank William G. Bousman of the U.S. Army Aeroflightdynamics Directorate (retired) for providing the TRCPCL pressure-integration code. They would also like to thank Robert M. Kufeld of NASA Ames for providing the flight data.

## References

[1]Sankaran, V., Potsdam, M., Wissink, A., Datta, A., Jayaraman, B., and Sitaraman, J., "Rotor Loads Predic-

tion in Level and Maneuvering Flight Using Unstructured-Adaptive Cartesian CFD," *American Helicopter Society 67th Annual Forum Proceedings*, 2011.

[2]Biedron, R. and Lee-Rausch, E., "Computation of UH-60A Airloads Using CFD/CSD Coupling On Unstructured Meshes," *American Helicopter Society 67th Annual Forum Proceedings*, 2011.

[3]Bousman, W. G. and Kufeld, R. M., "UH-60A Airloads Catalog," NASA TM 2005-212827, Aug. 2005.

[4]Anderson, W. K. and Bonhaus, D. L., "An Implicit Upwind Algorithm for Computing Turbulent Flows on Unstructured Grids," *Computers and Fluids*, Vol. 23, No. 1, 1994, pp. 1–22.

[5]http://fun3d.larc.nasa.gov, Last accessed 15 March, 2012.

[6]Biedron, R. T. and Thomas, J. L., "Recent Enhancements To The FUN3D Flow Solver for Moving Mesh Applications," AIAA Paper 2009-1360, Jan. 2009.

[7]Noack, R. W., "DiRTlib: A Library to Add an Overset Capability to Your Flow Solver," AIAA Paper 2005-5116, June 2005.

[8]Noack, R. W., Bogar, D. A., Kunz, R. F., and Carrica, P. M., "SUGGAR++: An Improved General Overset Grid Assembly Capability," AIAA Paper 2009-3992, June 2009.

[9]Biedron, R. T. and Lee-Rausch, E. M., "Rotor Airloads Prediction Using Unstructured Meshes and Loose CFD/CSD Coupling," AIAA Paper 2008-7341, Aug. 2008.

[10]Abras, J., *Enhancement of Aeroelastic Rotor Airloads Prediction Methods*, Ph.D. thesis, Georgia Institute of Technology, 2009.

[11]Potsdam, M., Yeo, H., and Johnson, W., "Rotor Airloads Prediction Using Aerodynamic/Structural Coupling," *American Helicopter Society 60th Annual Forum Proceedings*, 2004.

[12]Johnson, W., "Rotorcraft Aerodynamics Models for a Comprehensive Analysis," *American Helicopter Society 54th Annual Forum Proceedings*, 1998.

[13]Spalart, P. R. and Allmaras, S. R., "A One-Equation Turbulence Model for Aerodynamic Flows," *La Recherche Aerospatiale,* No. 1, 1994, pp. 5–21.

[14]Norman, T., Peterson, R., Shinoda, P., and Datta, A., "Full-Scale Wind Tunnel Test of the UH-60A Airloads Rotor," *American Helicopter Society 67th Annual Forum Proceedings*, 2011.

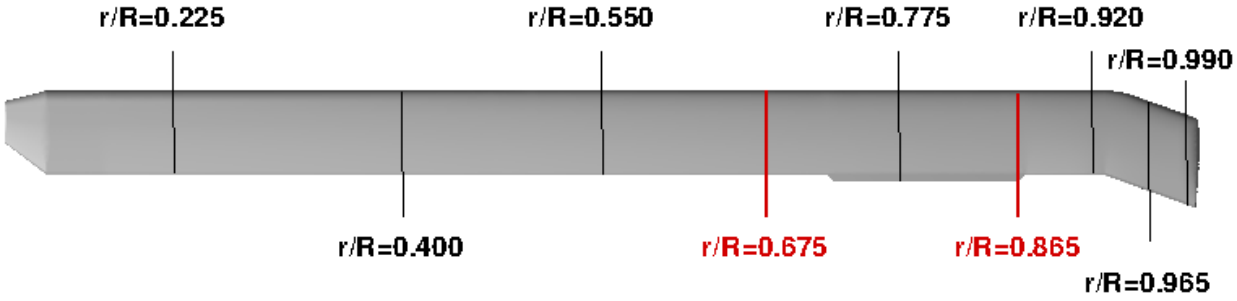


**Fig. 1. Blade radial stations at which pressures were measured where red indicates stations examined in this paper.**

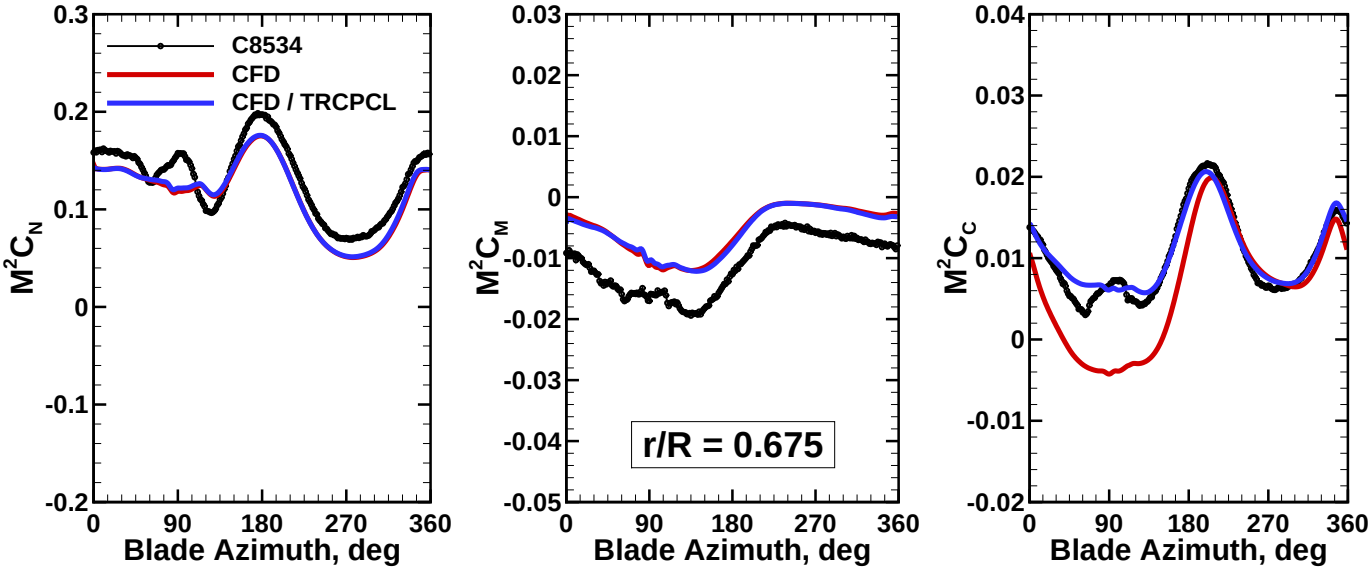


**Fig. 2. Comparison of computed and measured airloads at r/R = 0.675 for Counter 8535. Flight data and CFD via TRCPCL use identical integration of pressure and neglect skin friction.**

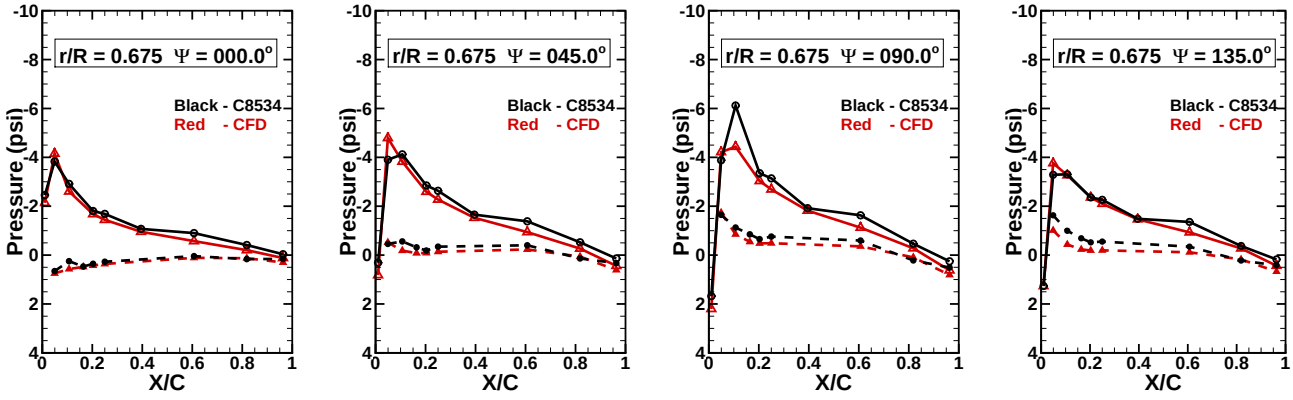


**Fig. 3. Comparison of computed and measured pressures at r/R = 0.675 for Counter 8534 on the advancing side (azimuthal increments of 45°; solid lines, upper surface; dashed lines, lower surface).**

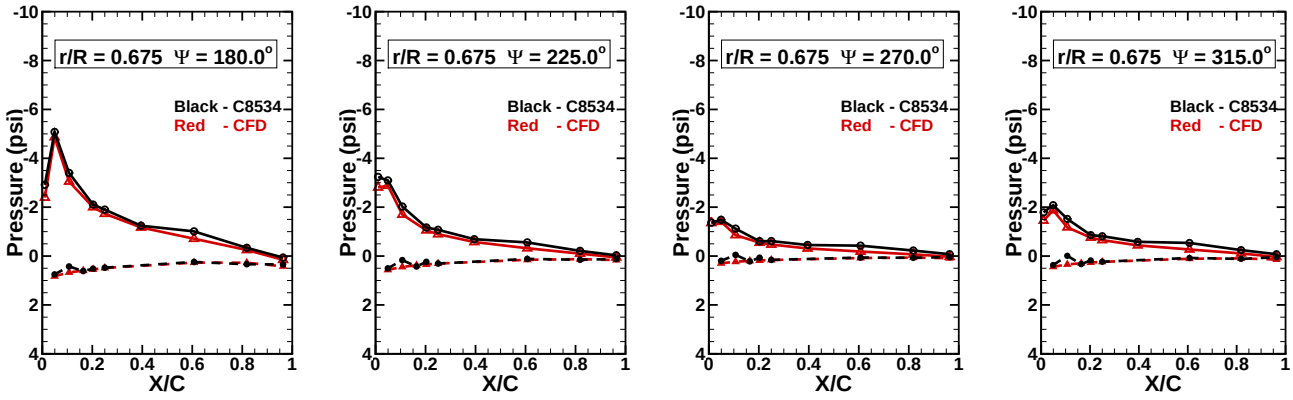


**Fig. 4. Comparison of computed and measured pressures at r/R = 0.675 for Counter 8534 on the retreating side (azimuthal increments of 45°; solid lines, upper surface; dashed lines, lower surface).**

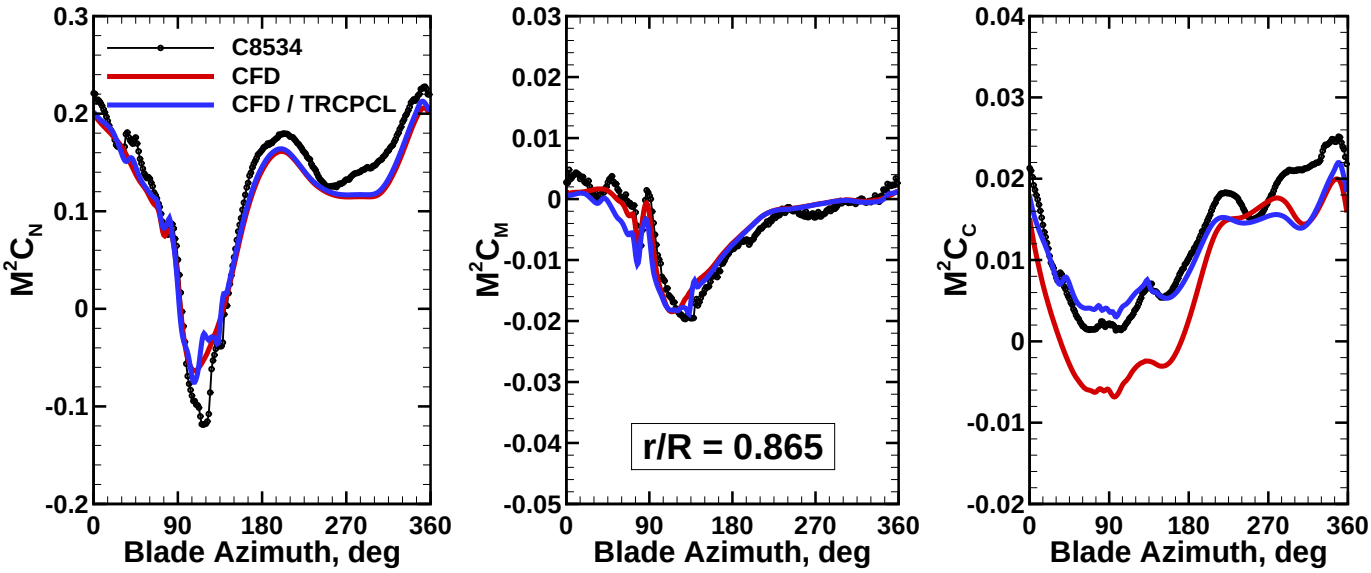


**Fig. 5. Comparison of computed and measured airloads at r/R = 0.865 for Counter 8534. Flight data and CFD / TRCPCL use identical integration of pressure and neglect skin friction.**

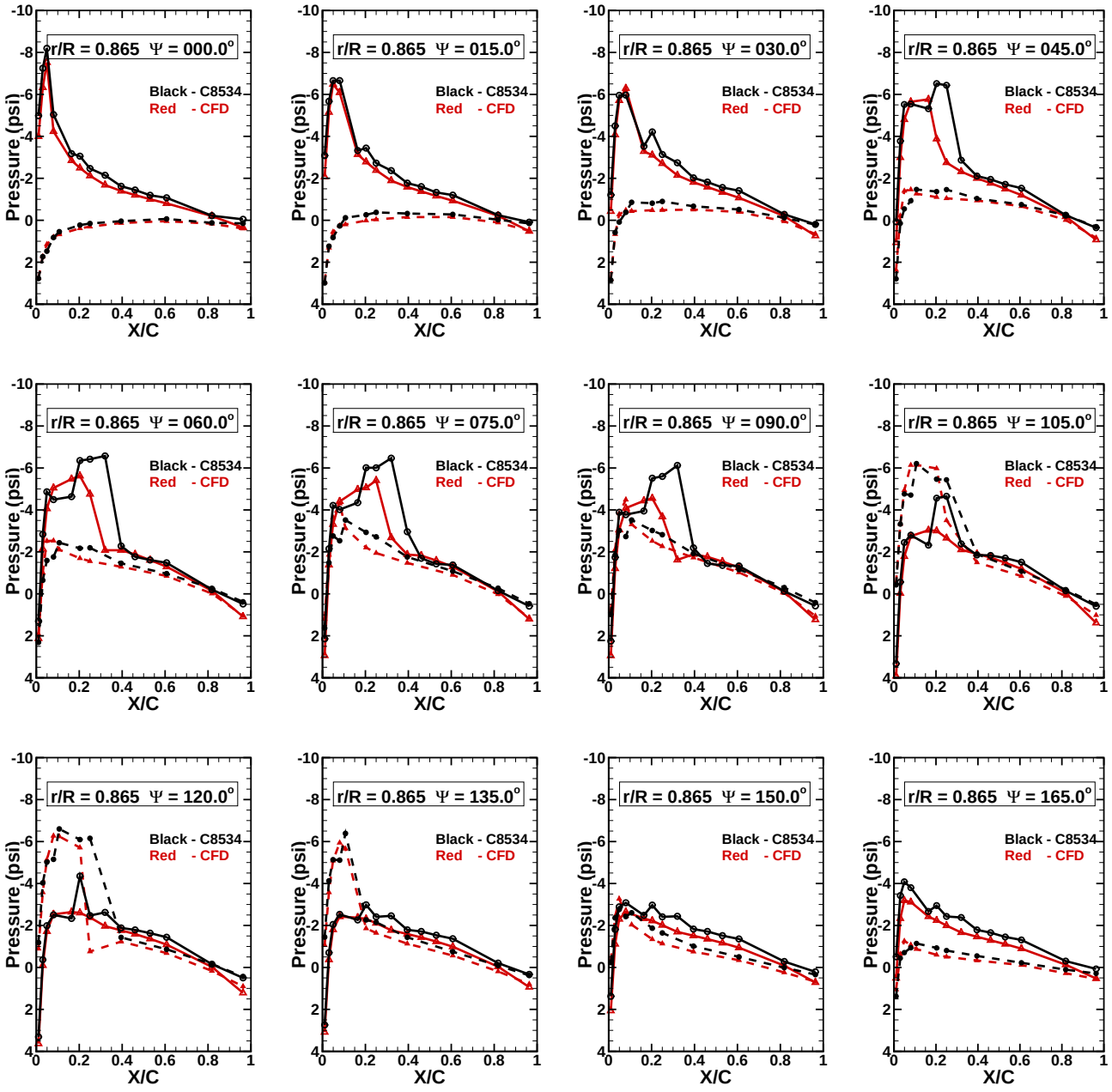


**Fig. 6. Comparison of computed and measured pressures at r/R = 0.865 for Counter 8534 on the advancing side (azimuthal increments of 15°; solid lines, upper surface; dashed lines, lower surface).**

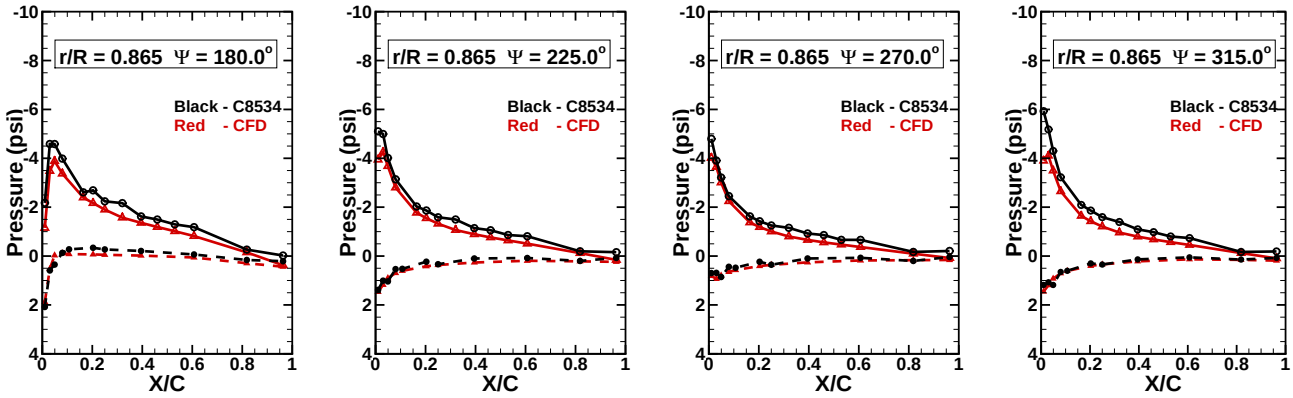


**Fig. 7. Comparison of computed and measured pressures at r/R = 0.865 for Counter 8534 on the retreating side (azimuthal increments of 45°; solid lines, upper surface; dashed lines, lower surface).**

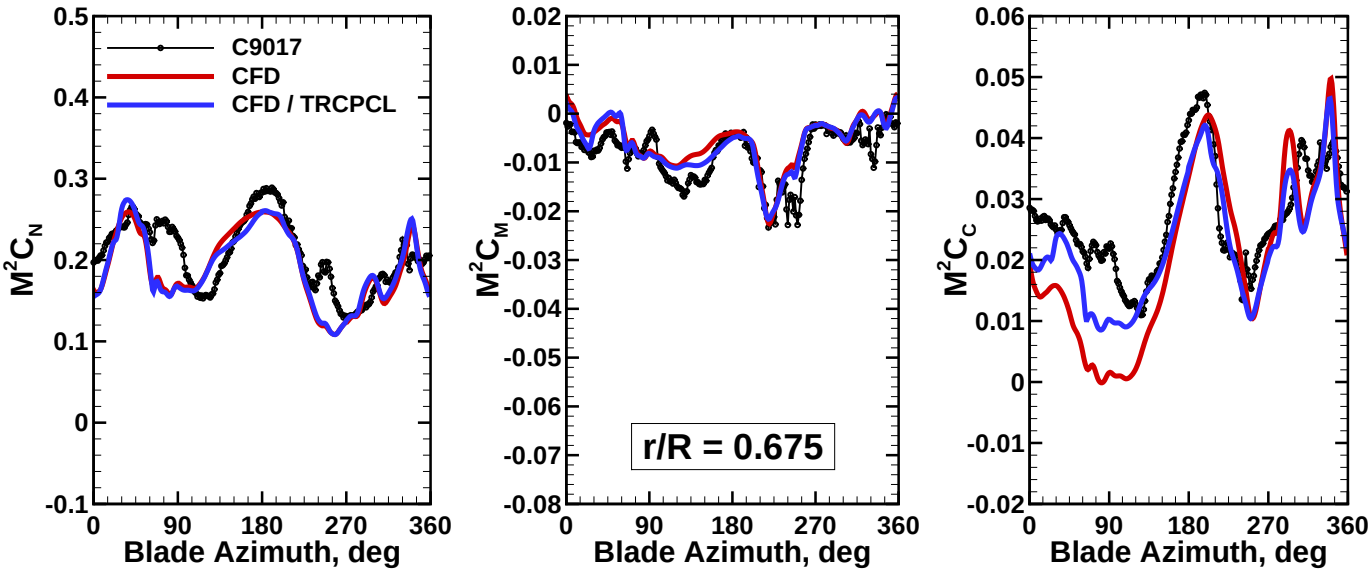


**Fig. 8. Comparison of computed and measured airloads at r/R = 0.675 for Counter 9017. Flight data and CFD via TRCPCL use identical integration of pressure and neglect skin friction.**

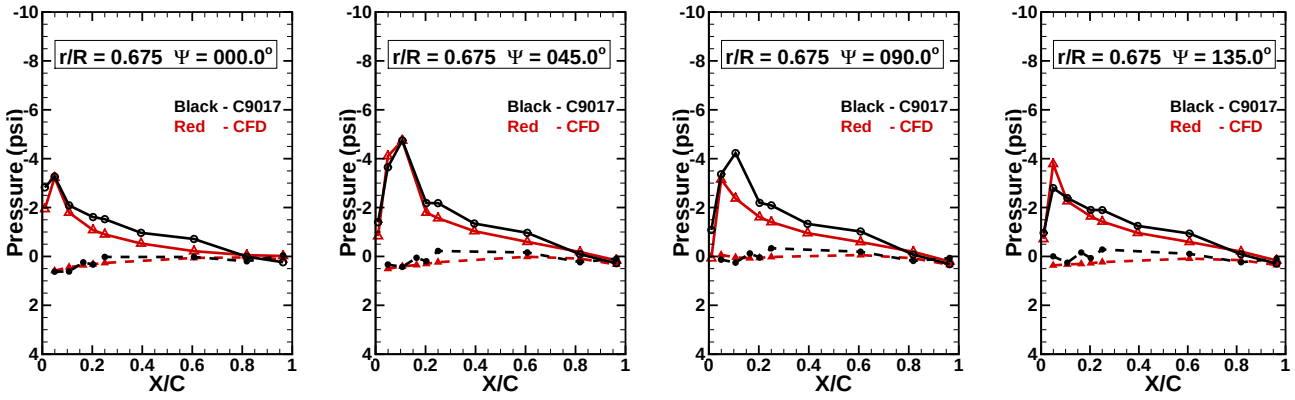


**Fig. 9. Comparison of computed and measured pressures at r/R = 0.675 for Counter 9017 on the advancing side (azimuthal increments of 45°; solid lines, upper surface; dashed lines, lower surface).**

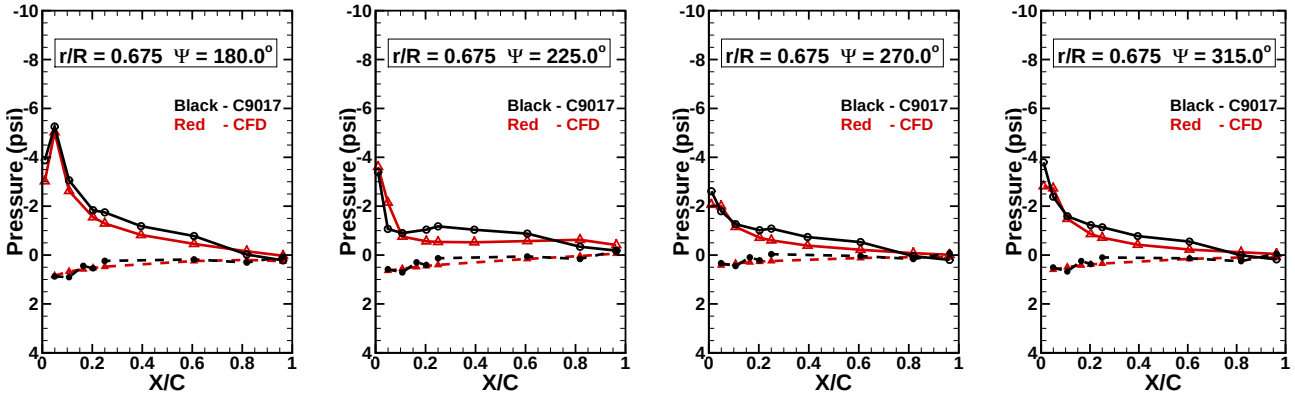


**Fig. 10. Comparison of computed and measured pressures at r/R = 0.675 for Counter 9017 on the retreating side (azimuthal increments of 45°; solid lines, upper surface; dashed lines, lower surface).**

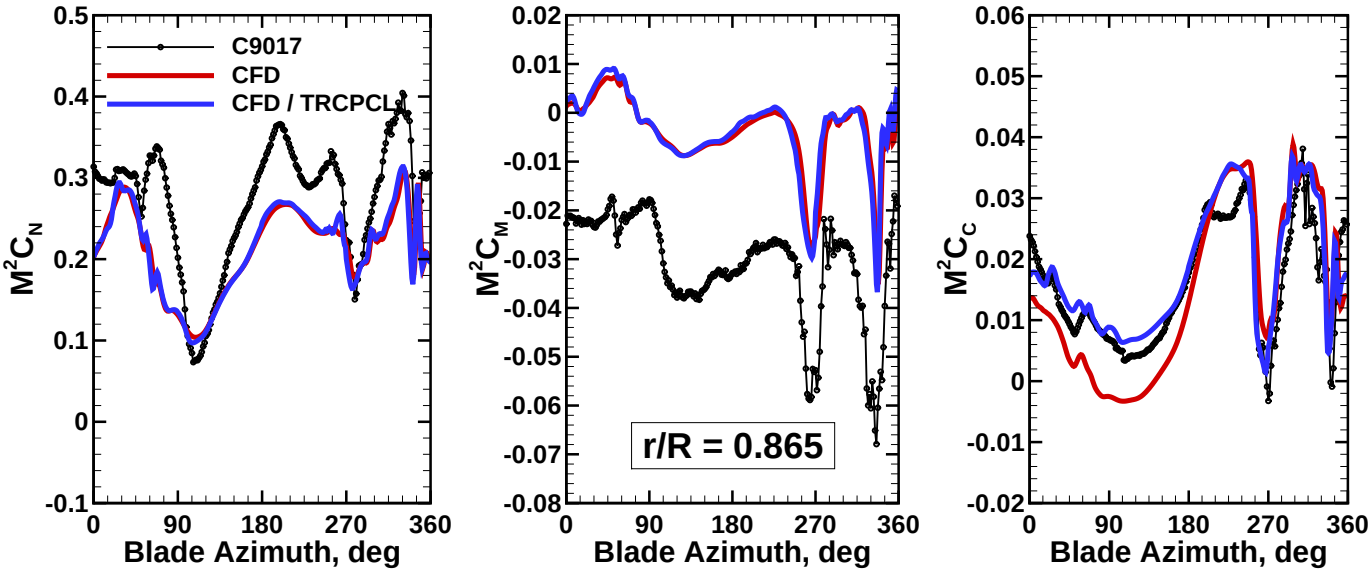


**Fig. 11. Comparison of computed and measured airloads at r/R = 0.865 for Counter 9017. Flight data and CFD / TRCPCL use identical integration of pressure and neglect skin friction.**

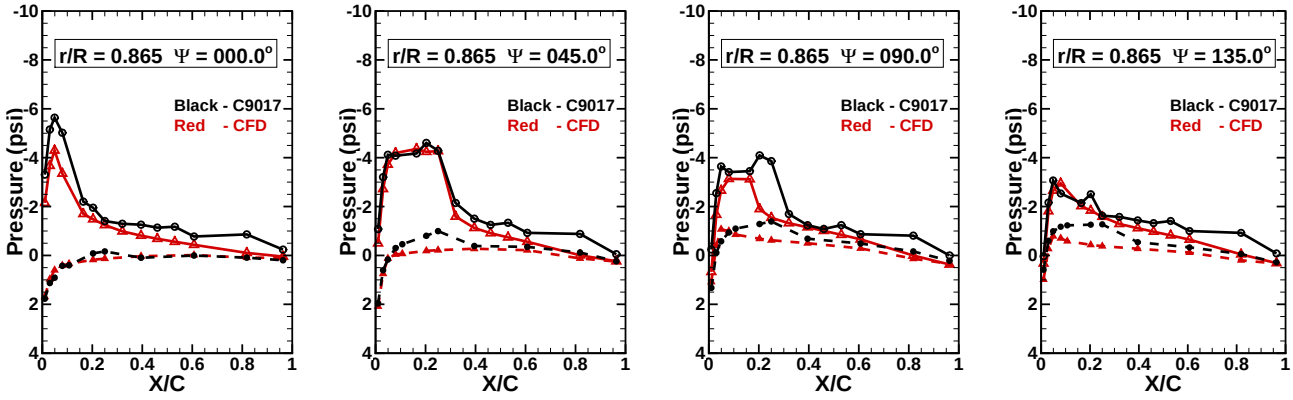


**Fig. 12. Comparison of computed and measured pressures at r/R = 0.865 for Counter 9017 on the advancing side (azimuthal increments of 45°; solid lines, upper surface; dashed lines, lower surface).**

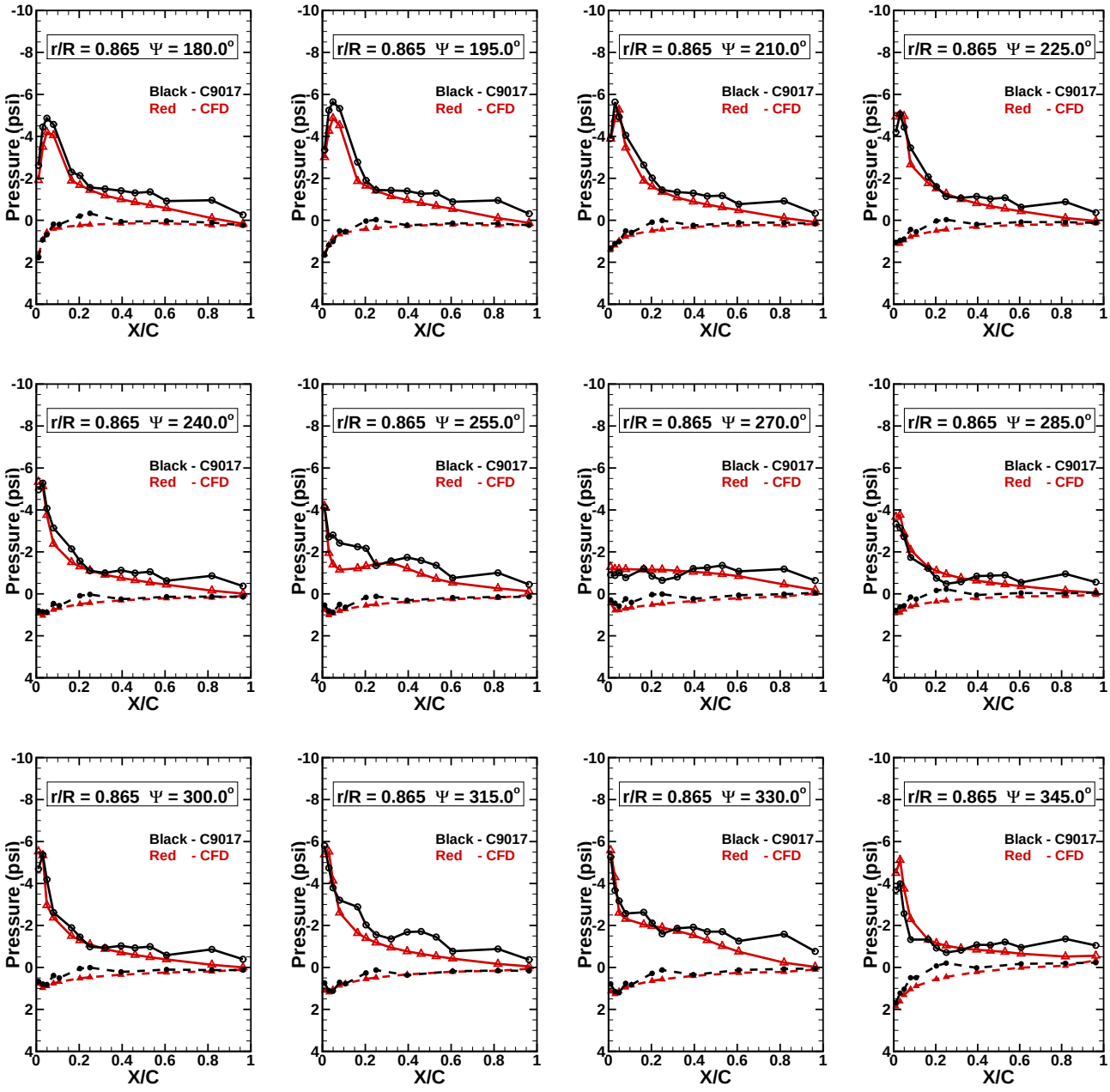


**Fig. 13. Comparison of computed and measured pressures at r/R = 0.865 for Counter 9017 on the retreating side (azimuthal increments of 15°; solid lines, upper surface; dashed lines, lower surface).**